frontiers | Frontiers in Electronics

TYPE Original Research
PUBLISHED 27 August 2024
DOI 10.3389/felec.2024.1369905

EDITED BY
Wenjie Liu,
Northwestern Polytechnical University, China

REVIEWED BY
Elena Helerea,
Transilvania University of Brașov, Romania
Zhihao Min,
Universitat Politecnica de Catalunya, Spain

*CORRESPONDENCE
Ming Zhao,
✉ mingzhao1226@163.com
Yang Liu,
✉ liuyang052126@163.com

RECEIVED 13 January 2024
ACCEPTED 18 July 2024
PUBLISHED 27 August 2024

CITATION
Hou L, Zhao M, Wang Y, Qu F, Shao D, Yang X, Liu Y and Yang Z (2024) Research on the energy transmission mode of a three-port DC–DC converter based on ultra-thin silicon steel.
Front. Electron. 5:1369905.
doi: 10.3389/felec.2024.1369905

Research on the energy transmission mode of a three-port DC–DC converter based on ultra-thin silicon steel

Lei Hou[1], Ming Zhao[2]*, Yixiao Wang[3], Feng Qu[1], Dan Shao[1], Xin Yang[1], Yang Liu[4]* and Zhaoning Yang[5]

[1]Xiong'an New Area Power Supply Company, State Grid Hebei Electric Power Co., Ltd., Xiong'an, China, [2]State Grid Hebei Sevice Center Co., Ltd., ShiJiaZhuang, China, [3]Shanghai Electric Power Design Institute Co., Ltd., Shanghai, China, [4]XJ Group Corporation, Xuchang, China, [5]Key Laboratory of Special Motors and High Voltage Electrical Appliances, Ministry of Education Shenyang University of Technology, Shenyang, China

With the introduction of China's "Carbon Peaking Action Plan Before 2030," the transformation of the power industry has released huge opportunities and potential. The DC distribution network can well-coordinate the contradiction between distributed power and grid access, fully develop the benefits of distributed energy, and become a new direction for the development of the power industry. However, the current traditional DC–DC converters have problems such as single-topology structure and low power density, which can only complete one-way transmission of energy; hence, the distributed energy cannot be fully utilized. Addressing the problem of distributed energy transfer, this paper is based on a three-port DC–DC converter for a low-voltage DC distribution network to realize energy transfer between the DC distribution network, distributed energy, and low-voltage load. First, the energy transfer modes of the three-port DC–DC converter are introduced. Combined with the converter topology and energy transfer mode, a simplified equivalent model of the converter is established. The voltage gain characteristics and frequency characteristics of this converter are studied. Furthermore, the effects of the excitation inductance to primary resonance inductance ratio parameter k and quality factor Q on the voltage gain characteristics of the converter are discussed. On this basis, the resonant cavity design of the converter is based on the optimal selection of parameters k and Q so that the converter can meet the voltage gain requirements in both forward and reverse operations. The simulation results under different loads verify the reasonableness of the resonant cavity component selection.

KEYWORDS
DC distribution network, three-port DC–DC converter, capacitor–inductor–inductor–inductor–capacitor resonant converter, decoupling equivalence, resonator design

1 Introduction

With the emergence of energy shortage and environmental pollution and the increasing demand for electricity and power quality, the traditional AC distribution network faces a series of problems in solving load diversification and reducing energy loss (Boroyevich et al., 2010; Zheng, 2014; Chen, 2017). In the field of electric power, DC distribution using new energy has become the only way for the transformation and upgrading of the traditional manufacturing industry (Tong et al., 2007; Song et al., 2013; Wu et al., 2013). In recent years, China has made great efforts to develop distributed renewable energy and clean energy technology (She et al., 2013). Distributed energy has the problems of scale, dispersion, indirection, and uncertainty (Ortiz, 2010; Bahmani et al., 2016). The DC distribution network can coordinate the contradiction between distributed power and grid access well and maximize the value and benefit of distributed energy (Villar et al., 2008; Villar et al., 2009). At the same time, the DC distribution network is superior to the AC distribution network in voltage grade, control system, and equipment cost and has flexible scheduling function. Therefore, a low-voltage DC power distribution network will be the trend for future development (Heinemann, 2002; Soltau et al., 2014; Zhao et al., 2021).

The topological structure of the three-port DC–DC converter is shown in Figure 1. U_{in} is connected to 380 V AC and outputs 537 V DC voltage by PFC rectification. U_{out} is connected to a 375-V distributed energy storage system; R_0 is connected to a 48 V low-voltage load. The DC bus and distributed energy storage system constitute a capacitor–inductor–inductor–inductor–capacitor (CLLLC) bidirectional DC–DC converter to achieve bidirectional energy flow. The isolation transformer uses a three-winding core structure for ensuring that the voltage supplied by the DC bus adequately meets the requirements of both the distributed energy storage system and low-voltage loads. Furthermore, the topology has the capacity to improve the power density and concurrently diminish the volumetric dimensions of the converter. The bidirectional CLLLC resonator ensures zero voltage on and zero current off of the switching device, further saving energy. The basic parameters of the three-port DC-DC converter and three-winding intermediate frequency transformer are shown in Table 1.

2 Analysis of the energy transmission mode of the converter

In the topology of the three-port DC–DC converter, the three-winding transformer is the core component of the converter's energy transmission. The isolation transformer is used for energy transmission and conversion. The specific working mode can be divided into three types, as shown in Figure 2.

Energy transmission mode 1 is the 537-V DC bus to charge mode, power flow from the DC bus side to a 375-V distributed energy storage system, and 48 V low-voltage load, which can be equivalent to a CLLLC bidirectional resonant converter and one-way LLC converter running in parallel; the DC bus port and distributed energy storage port constitute the CLLLC resonant topology of forward operation. The DC bus port and the low-voltage load port form a unidirectional LLC resonant topology. Energy transmission mode 2 is the distributed energy storage feedback DC bus mode. The power flows from the 375 V distributed energy storage side to the 537 V DC bus side, and the energy in distributed energy storage is injected into the grid. In this case, the three-port converter is a CLLLC full-bridge circuit operating in reverse, and the low-voltage 48-V load does not participate in energy transmission. Energy transmission mode 3 is the 375-V distributed energy storage system charging a low-voltage 48-V load, and the power flows from the distributed energy

TABLE 1 Parameters of the three-port DC–DC converter.

Parameter	Numerical value
Rated input voltage U_{in}	537 V
Rated output voltage U_{out1}	375 V
Rated output voltage U_{out2}	48 V
Output power P_0	20 kW
Operation frequency f_s	20 kHz
Maximum operating flux B_m	0.5 T
Efficiency η	96%
Maximum current density J	200 A/cm^2

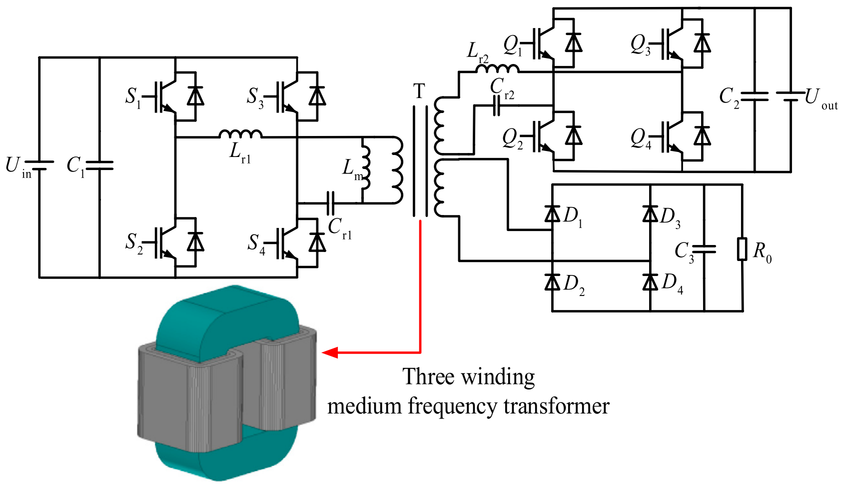

FIGURE 1
Three-port DC–DC resonant converter topology.

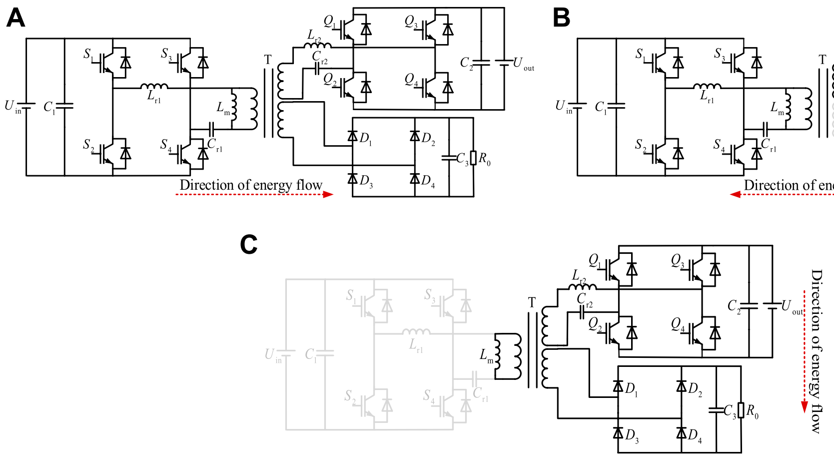

FIGURE 2
Three-port DC–DC converter energy transfer modes: **(A)** energy transmission mode 1; **(B)** energy transmission mode 2; **(C)** energy transmission mode 3.

storage side to the low-voltage load side, which can be equivalent to a one-way full-bridge LLC circuit.

There are two resonant frequencies in the converter's forward operation. The first resonant frequency is generated by the resonance of the front resonant cavity elements L_{r1} and C_{r1}. The second resonant frequency is generated by the resonance between excitation inductor L_m and front resonant cavity elements L_{r1} and C_{r1}, which can be expressed as Equations 1, 2.

$$f_{r1} = \frac{1}{2\pi\sqrt{L_{r1}C_{r1}}}, \tag{1}$$

$$f_m = \frac{1}{2\pi\sqrt{(L_{r1}+L_m)C_{r1}}}. \tag{2}$$

The output voltage is controlled by controlling the switching frequency. According to the different resonant frequencies, they are divided into three resonant working states: under-resonant $f_m < f_s < f_r$, quasi-resonant $f_s = f_m$, and over-resonant $f_s > f_r$.

When the three-port DC–DC converter operates forward, it can be divided into three parts: port 1 is four IGBTs that constitute the inverter unit, port 2 is four IGBTs that constitute the rectifier unit, and port 3 is four diodes that constitute the uncontrolled rectifier unit. C_1 and C_2 are filtering capacitors in the forward and reverse operations, respectively, and C_3 is a filtering capacitor of port 3. L_{r1} and C_{r1} are the resonant inductor and the resonant capacitor at the input stage of the forefront section, respectively. L_m is the excitation inductance of the transformer. L_{r2} and C_{r2} are the resonant inductors and capacitors of the later stage, respectively. In order to avoid the influence of some parasitic parameters on the working state of the converter, the converter is assumed to be in stable running state first. The switching device is an ideal type device. The initial energy storage of the inductor and capacitor is 0. The filter capacitor is large enough; the output voltage is the voltage source. The forward operation of the converter can be divided into eight stages, among which the first four stages and the last four stages are completely symmetric. In order to facilitate the description of the working process, the switching tube dead time is increased. This paper only analyzes the converter's working process under the first four time states. The working waveform under the under-resonant state is shown in Figure 3. As shown in Figure 3, the switching tube dead time is large, which can be more intuitive to observe the working process of the converter, and the actual dead time is far less than the period in the figure.

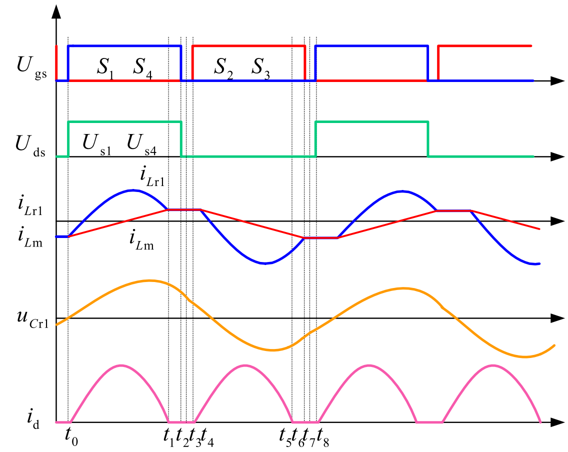

FIGURE 3
Waveforms of the converter in the under-resonance region.

Stage 1 (t_0–t_1): Before t_0, the resonator is in a resonant state, and the switching tubes S_2 and S_3 are closed. The resonant current is continued through S_1 and S_4 parallel diodes so that the voltage of the switching tubes S_1 and S_4 is reduced to 0. At t_0, S_1 and S_4 are switched on, and ZVS is switched on because the voltage of S_1 and S_4 is 0. In the t_0-t_1 stage, the direction of the resonator current i_{Lr1} decreases gradually, opposite to the reference direction, and changes with the sine rule; the direction of the current i_{Lm} in the excitation inductor L_m with the common reference direction increases gradually linearly with time. Since i_{Lr1} changes faster than i_{Lm}, energy is transferred from the input side to the output side through the induced current of the medium frequency transformer. Switch tubes Q_2 and Q_3 and

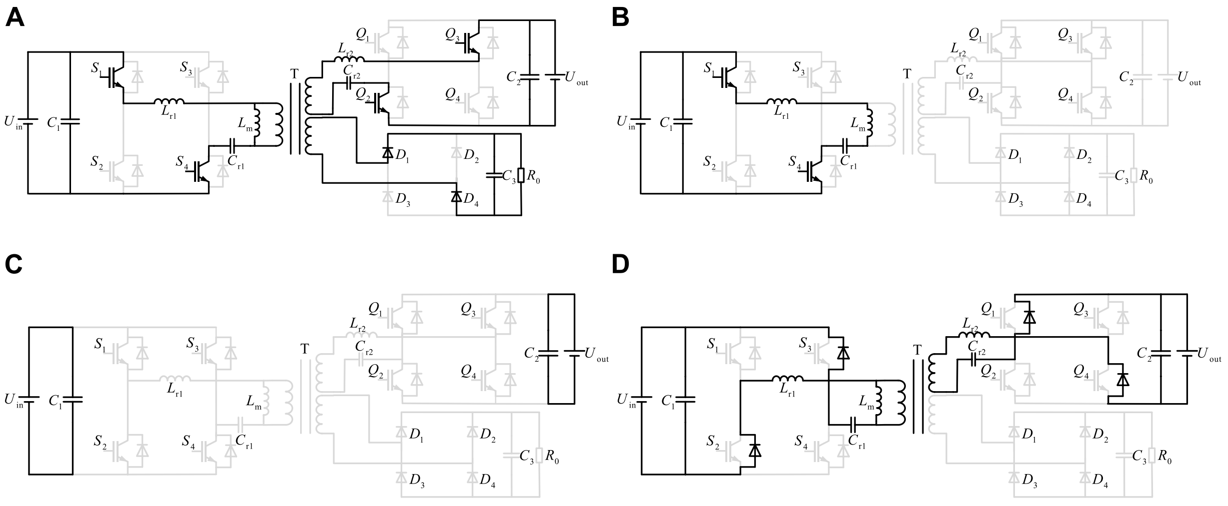

FIGURE 4
Under-resonant operating condition at $f_m < f_s < f_r$: **(A)** stage 1 (t_0–t_1); **(B)** stage 2 (t_1–t_2); **(C)** stage 3 (t_2–t_3); **(D)** stage 4 (t_3–t_4).

diodes D_1 and D_4 switch on. In this stage, the resonant inductor current i_{Lr1} and the excitation inductor current i_{Lm} change from negative to positive until they are equal at the end of this stage. At stage 1, the front resonant inductor L_{r1}, resonant capacitor C_{r1}, the side resonant inductor L_{r2}, and resonant capacitor C_{r1} all participate in the resonant process, while L_m does not participate. This stage is shown in Figure 4A.

Stage 2 (t_1–t_2): At time t_1, switch tubes S_1 and S_4 are still on, and the resonant inductor current i_{Lr1} is equal to the excitation inductor current i_{Lm}. The input current of this medium-frequency transformer is 0, and switch tubes at the secondary side will be automatically shut down as the input current is 0 so that the ZCS is turned off and the power reflux problem avoided. This stage is shown in Figure 4B.

Stage 3 (t_2–t_3): At time t_2, switch tubes S_1 and S_4 are closed and are in the off state when they enter the dead zone. The voltage of switch tubes S_1 and S_4 is the input voltage U_{in}, as shown in Figure 4C.

Stage 4 (t_3–t_4): At time t_3, switch tubes S_2 and S_3 have zero potential, the resonant current follows the current along the parallel diodes, and the output voltage of the front resonator is U_{in}. At this time, switch tubes S_2 and S_3 can realize ZVS switch-off and reasonably design the dead time to ensure that switch tubes are ZVS on and ZCS off. At time t_4, switch tubes S_2 and S_3 switch on, and at the first half cycle of time t_1–t_4, switch tubes S_2 and S_3 switch off, as shown in Figure 4D.

Since the input side switch tubes S_1–S_4 and output side switch tubes Q_1–Q_4 adopt the same duty cycle control mode, which in the t_0–t_4 mode and t_4–t_8 mode are completely symmetric when the three-port converter is running forward, this paper will not describe it in detail. Theoretically, in order to improve the efficiency of the resonant converter and reduce the switching tube loss, the converter needs to operate in the under-resonant region because of the over-resonant region problem. The parametric design of a single-directional LLC is easy to implement. Although the structure of port 1 and port 2 of the bidirectional three-port resonant converter is symmetric and the work principle is the same, the under-resonant region of port 1 and the resonant region of port 2 will overlap when port 2 runs in reverse; when port 1 forward operates in the full voltage range of the under-resonant region, port 2 reverse operates in the over-resonant region. When port 1 and port 2 operate in the same voltage range, it is almost impossible to achieve under-resonance in both positive and negative operation modes. The resonant frequency in reverse operation can be optimized by the reasonable design of resonant cavity operating parameters so as to reduce the switching tube loss caused by over-resonant operation.

3 Analysis of the converter decoupling equivalent model

The three-port DC–DC converter requires different power transmission branches in different operation modes. A simplified equivalent circuit model is adopted to study the power flow relationship between the three ports of the converter. The influence of leakage inductance and coupling capacitance, stray inductance of the circuit, and filter capacitance of the medium-frequency transformer is ignored in the equivalent model. The equivalent model is shown in Figure 5.

In Figure 5B, L'_{r2} and C'_{r2} are the resonant inductance and resonant capacitor converted from the secondary side to the primary side of the converter, respectively. U_1 is the input square wave voltage at the primary side of the resonator. U_2 and U_3 are the output square wave voltages of the secondary side of the converter. U'_2 and U'_3 are from the secondary side converted to the primary side equivalent square wave voltages of the converter. The voltage parameters on the primary and secondary sides and resonant inductance and capacitance of the resonator after conversion are shown in Equations 3, 4.

$$\begin{cases} U_2' = U_2 n_1 / n_2 \\ U_3' = U_3 n_1 / n_3 \end{cases}, \tag{3}$$

$$\begin{cases} L_{r2}' = \dfrac{L_{r2}}{(n_1/n_2)^2} \\ C_{r2}' = C_{r2}(n_1/n_2)^2 \end{cases}. \tag{4}$$

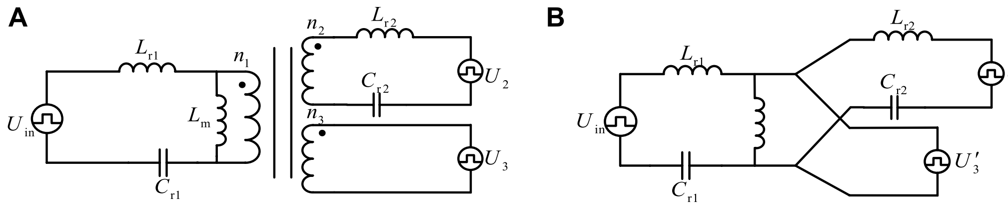

FIGURE 5
Equivalent circuit of the three-port DC–DC converter. **(A)** Converter equivalent model. **(B)** Converter Y-type equivalent model.

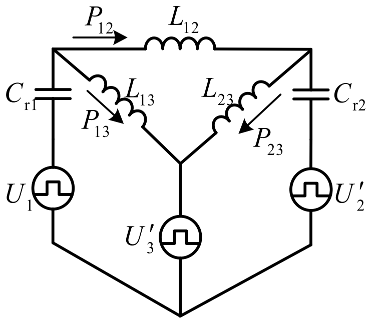

FIGURE 6
△-type equivalent circuit.

We suppose that the equivalent parallel point voltage of the three-port medium-frequency transformer is U_0. After the AC voltage of the three-port transformer transmits power through the respective ports, a common voltage U_0 can be formed in the medium-frequency transformer equivalent model. The resonant inductance of the resonator is much larger than the excitation inductance of the medium-frequency transformer. In order to expediently analyze, the role of the transformer excitation inductance is ignored. The △-type equivalent circuit obtained by the Y-△ transformation of the Y-type equivalent circuit in Figure 5B is shown in Figure 6.

In Figure 6, L_{12}, L_{13}, and L_{32} are energy transfer inductors between ports. According to the Y-△ transformation equation, the inductance expression of the △-type equivalent circuit can be written as Equation 5.

$$\begin{cases} L_{12} = L_{r1} + L'_{r2} \\ L_{13} = L_{r1} \\ L_{23} = L'_{r2} \end{cases}. \tag{5}$$

The energy transfer between port 1 and port 2 is only related to the resonant inductors L_{r1} and L_{r2} of port 1 and port 2 and resonant capacitors C_{r1} and C_{r2} from Figure 5 but has no coupling relationship with port 3. Similarly, when charging the low-voltage load of port 3, ports 1 and 2 are only related to the resonant device of the port itself, and there is no coupling relationship between ports. Therefore, the three-port DC–DC converter can be equivalent to the simplified circuit model shown in Figure 7.

The energy transfer between the ports of the three-port converter is based on the ideal state, and the leakage inductance of the medium frequency transformer will generate cyclic power between the ports in the actual operation process, which can only be eliminated by modulation technology. Port 1 and port 2 can eliminate the cyclic power by the modulation technology. In contrast, port 3 can reduce the cyclic power of the converter only by minimizing the primary-side leakage inductance of the medium-frequency transformer as port 3 is the full-bridge uncontrolled rectifier circuit. The CLLLC resonant converter is mainly divided into three parts, the inverter side, the resonator side, and the rectifier side, as shown in Figure 8.

The converter-simplified equivalent circuit can be considered a bidirectional CLLLC converter and a unidirectional LLC converter running side by side. The forward operation principle of the bidirectional CLLLC converter is the same as that of the LLC converter. This paper considers the forward operation of the CLLLC converter as an example to analyze the frequency characteristics and voltage gain characteristics between port 1 and port 2 of the three-port converter. The resonant converter usually works near the resonant frequency point. The first harmonic analysis (FHA) method is used to decompose the square wave voltage input to the resonator by Fourier decomposition. The harmonic component is ignored. Assume that only the fundamental component completes the energy transmission of the resonant converter.

The drive signals of switch tubes S_1 and S_4 on the inverter side are complementary to the drive signals of switch tubes S_2 and S_3, and the switch tubes are conducted alternately. The input voltage at both ends of the resonator is the square wave voltage from U_{in} to U_{in}. U_{AB} varies with the switching tube period, as shown in Equation 6. The resonator, a filter network with frequency-selective properties, weakens the higher harmonics. The resonator input voltage U_{AB} mainly depends on the input voltage U_{in} and the fundamental component of input current i_{r1} of the converter.

$$u_{AB}(t) = \begin{cases} U_{in} \left(0 < t < \dfrac{T_s}{2}\right) \\ -U_{in}\left(\dfrac{T_s}{2} < t < T_s\right) \end{cases}, \tag{6}$$

where U_{in} is the input voltage of the converter; T_s is the switching cycle.

Taking Fourier transform of Equation 6, Equation 7 can be obtained as follows.

$$u_{AB}(t) = \frac{4U_{in}}{\pi} \sum_{n=1,3,5\ldots} \frac{1}{n} sin\left(2\pi n f_s t\right). \tag{7}$$

The equivalent resistance R_{eq} at the input of the resonator is expressed as Equation 8.

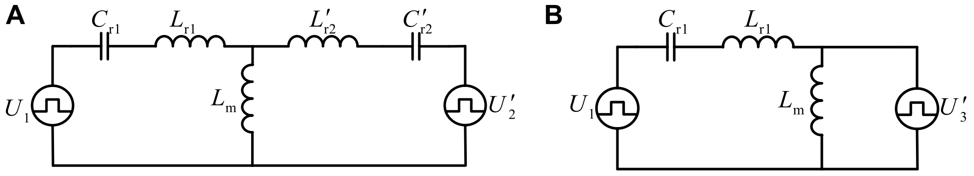

FIGURE 7
Simplified equivalent circuit model: **(A)** equivalent model for ports 1 and 2; **(B)** equivalent model for ports 1 and 3.

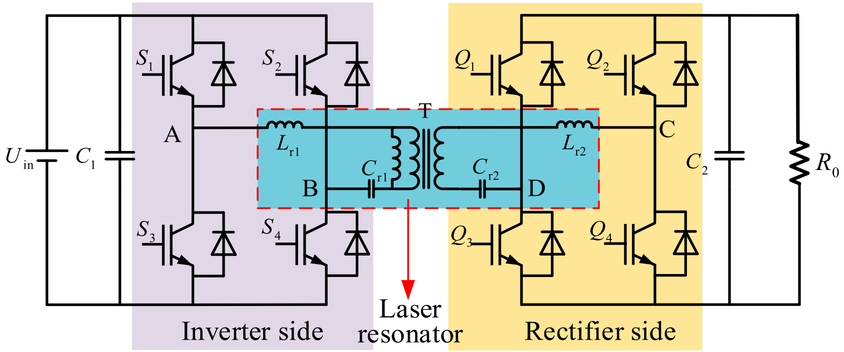

FIGURE 8
CLLLC resonant converter.

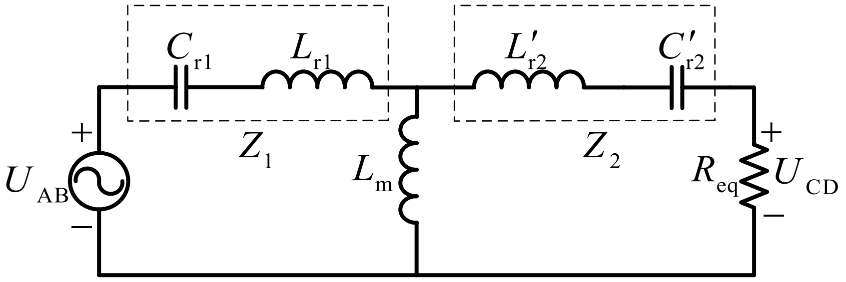

FIGURE 9
Port 1 and port 2 FHA equivalent model.

$$\boldsymbol{R_{eq}} = \frac{\boldsymbol{U_{p1}}}{\boldsymbol{I_{p1}}} = \frac{\boldsymbol{8n^2}}{\boldsymbol{\pi^2}}\boldsymbol{R_0}. \tag{8}$$

The simplified equivalent model of the converter after fundamental equivalent analysis is shown in Figure 9.

The main circuit of port 1 and port 2 of the three-port DC–DC converter is simplified into a purely resistive load resonant network driven by a sinusoidal fundamental voltage by the fundamental wave analysis method. The resonant frequency characteristics and voltage gain characteristics can be solved by the fundamental equivalent circuit based on port 1 and port 2.

4 Characteristic analysis of the three-port DC–DC converter

4.1 Resonance frequency analysis

The resonant converter changes the resonant cavity equivalent input impedance by changing the operating frequency to control the output voltage. Figure 9 shows the fundamental equivalent model between port 1 and port 2 of the converter. The resonator parameters are further defined as follows:

$$\begin{cases} Z_1 = j\omega_s L_{r1} + 1\big/\left(j\omega_s C_{r1}\right) \\ Z_2 = j\omega_s L_{r2}' + 1\Big/\left(j\omega_s C_{r2}'\right) \\ Z_m = j\omega_s L_m \\ Z_{eq} = R_{eq} = 8n^2 R_0\big/\pi^2 \end{cases}, \tag{9}$$

where ω_s is the switching angular frequency $\omega_s = 2\pi f_s$; U_{AB} and U_{CD} are the input and output fundamental voltage of the resonator, respectively.

The resonator fundamental equivalent transfer function can be expressed as

$$H_r(j\omega_s) = \frac{U_{CD}}{U_{AB}} = \frac{Z_m//(Z_2+Z_{eq})}{Z_1 + Z_m//(Z_2+Z_{eq})}\cdot\frac{Z_{eq}}{Z_2+Z_{eq}}. \tag{10}$$

Substituting Equation 9 into Equation 10,

$$H_r(j\omega_s) = \omega_s L_m R_{eq}\Bigg/\left[\left(\omega_s L_{r1} - \frac{1}{\omega_s C_{r1}} + \omega_s L_m\right)R_{eq} + j\left(\begin{array}{c}\omega_s^2 L_{r1}L_m + \omega_s^2 L_{r2}' L_m + \omega_s^2 L_{r1}L_{r2}' \\ -\dfrac{L_m}{C_{r1}} - \dfrac{L_m}{C_{r2}'} - \dfrac{L_{r2}'}{C_{r1}} - \dfrac{L_{r1}}{C_{r2}'} + \dfrac{1}{\omega_s^2 C_{r1}C_{r2}'}\end{array}\right)\right]. \tag{11}$$

$k = L_m/L_{r1}$, $h = n_2 L_{r2}/L_{r1}$, and $g = C_{r2}/n_2 C_{r1}$; the normalized parameters k, h, and g are substituted into Equation 11:

$$H_r(j\omega_s) = k\omega_s C_{r1}R_{eq}\Bigg/\left[\left(\omega_s C_{r1} - \frac{1}{\omega_s L_{r1}} + k\omega_s C_{r1}\right)R_{eq} + j\left(\begin{array}{c}k\dfrac{\omega_s^2}{\omega_1^2} + kh\dfrac{\omega_s^2}{\omega_1^2} + h\dfrac{\omega_s^2}{\omega_1^2} - k \\ -\dfrac{k}{g} - h - \dfrac{1}{g} + \dfrac{1}{g}\dfrac{\omega_1^2}{\omega_s^2}\end{array}\right)\right]. \tag{12}$$

The numerator and denominator are multiplied by C_{r1}/L_{r1}; substituting $\omega_2 = \frac{1}{\sqrt{L_{r2}C_{r2}}} = \frac{\omega_1}{\sqrt{hg}}$ into Equation 12,

$$H_r(j\omega_s) = k\omega_s C_{r1}R_{eq}\Bigg/\left[\left(\omega_s C_{r1} - \frac{1}{\omega_s L_{r1}} + k\omega_s C_{r1}\right)R_{eq} + j\left(\begin{array}{c}k\dfrac{\omega_s^2}{\omega_1^2} + kh\dfrac{\omega_s^2}{\omega_1^2} + h\dfrac{\omega_s^2}{\omega_1^2} - k \\ -\dfrac{k}{g} - h - \dfrac{1}{g} + \dfrac{1}{g}\dfrac{\omega_1^2}{\omega_s^2}\end{array}\right)\right]. \tag{13}$$

When the resonator generates resonance, the imaginary part of the transfer function is 0. If the imaginary part in Equation 13 is equal to 0, then

$$k\frac{\omega_s^2}{\omega_1^2} + kh\frac{\omega_s^2}{\omega_1^2} + h\frac{\omega_s^2}{\omega_1^2} - k - \frac{k}{g} - h - \frac{1}{g} + \frac{1}{g}\frac{\omega_1^2}{\omega_s^2} = 0. \tag{14}$$

When the resonator generates resonance frequency ω_r, it is substituted into Equation 14, and both $\omega_1{}^2\omega_r{}^2$ are multiplied:

$$(k + kh + h)\omega_r^4 - \left(k + \frac{k}{g} + h + \frac{1}{g}\right)\omega_1^2\omega_r^2 + \frac{1}{g}\omega_1^4 = 0. \tag{15}$$

$a = k + kh + h$, $b = k + k/g + h + 1/g$, and $c = 1/g$; we can obtain

$$a\omega_r^4 - b\omega_1^2\omega_r^2 + c\omega_1^4 = 0. \tag{16}$$

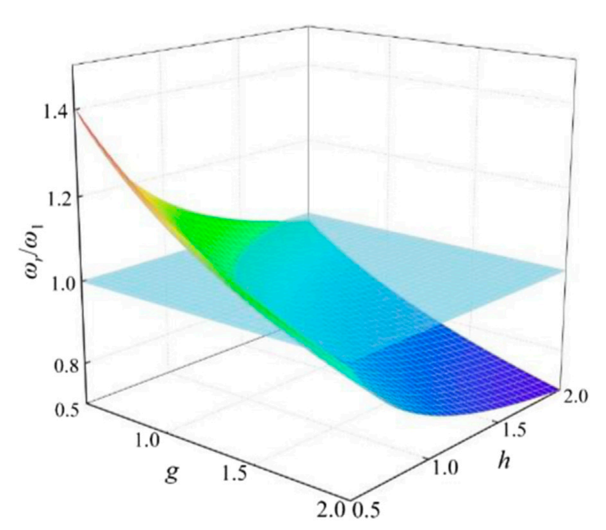

FIGURE 10
Resonant frequency ω_r/ω_1 versus g and h.

It can be obtained by solving Equation 16:

$$\omega_r^2 = \frac{b \pm \sqrt{b^2 - 4ac}}{2a}\cdot\omega_1^2. \tag{17}$$

When the resonator produces resonance, the series resonance frequency is greater than that of parallel resonance because the excitation inductance is greater than that of resonance inductance, $L_m > L_{r1}$. Therefore, the positive value of the normalized resonance frequency in Equation 17 is shown in Equation 18:

$$\frac{\omega_r}{\omega_1} = \sqrt{\frac{b + \sqrt{b^2 - 4ac}}{2a}}. \tag{18}$$

According to Equations 15, 18, the corresponding relationship between ω_r/ω_1 and the normalized parameters g and h can be drawn, which is shown in Figure 10. Through the space surface and $\omega_r/\omega_1 = 1$, the magnitude relationship of the resonant frequencies ω_1, ω_2, and ω_r is judged as shown in Equation 19:

$$\begin{cases} \omega_2 < \omega_r < \omega_1, h\cdot g > 1 \\ \omega_1 < \omega_r < \omega_2, h\cdot g < 1 \\ \omega_1 = \omega_r = \omega_2, h\cdot g = 1 \end{cases}. \tag{19}$$

Equation 19 and Figure 10 show that when the three-port DC–DC converter runs forward, the resonant inductor L_{r2} and the resonant capacitor C_{r2} of the output side of the resonators at ports 1 and 2 will affect the resonant frequency ω_r, which make the resonant frequency ω_r between ω_1 and ω_2. If ω_1 and ω_2 are equal, then the resonant frequency ω_r is equal to both of them $\omega_1 = \omega_2 = \omega_r$. As a result of the symmetric structure of the forward and reverse operation modes, the frequency characteristics of the resonant converter in reverse operation are the same. Theoretically speaking, the principle of the CLLLC resonant converter is the same as that of a conventional unidirectional LLC resonant converter, which also has three resonant states. The efficiency in the design of the converter can be improved by designing the converter in the state of under-resonance or quasi-resonance.

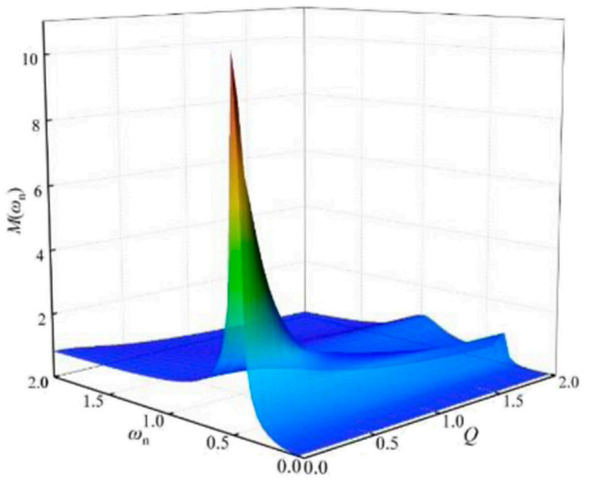

FIGURE 11
Voltage gain M versus Q and ω_n.

4.2 Analysis of voltage gain characteristics

The gain characteristics of the resonant converter are deduced and analyzed by using the fundamental analysis method FHA mentioned in the previous section. According to Equation 13, the characteristic impedance $Z_r = \sqrt{L_{r1}/C_{r1}}$, the quality factor $Q = Z_r/Z_{eq}$, and the normalized frequency $\omega_n = \omega_s/\omega_1$; the resonator transfer functions are obtained as follows:

$$H_r(j\omega_n) = \frac{1}{j\frac{Q}{k}\left((k+h+kh)\omega_n - \left(k+\frac{k}{g}+h+\frac{1}{g}\right)\frac{1}{\omega_n}+\frac{1}{g\omega_n^3}\right) + 1 + \frac{1}{k} - \frac{1}{k\omega_n^2}} \tag{20}$$

The simplified voltage gain expression can be obtained from Equation 20:

$$M(\omega_n) = \frac{1}{\sqrt{\left(1+\frac{1}{k}-\frac{1}{k\omega_n^2}\right)^2 + \left(\frac{Q}{k}\right)^2\left(a\omega_n - b\frac{1}{\omega_n} + c\frac{1}{\omega_n^3}\right)^2}}. \tag{21}$$

When the switching frequency and resonant frequency of the converter are equal, $\omega_s = \omega_r$, the expression ω_r is incorporated into Equation 21. According to the resonant frequency, $a\omega_r$-b/ω_r + c/ω_{r3} = 0, and the simplified voltage gain is shown in Equation 22:

$$M(\omega_r) = \frac{1}{1+\frac{1/g-h}{k+k/g+h}}. \tag{22}$$

According to Equation 18, when the resonant frequency $\omega_r/\omega_1 = 1$, the voltage gain of the converter is independent of the load, and the voltage gain M of Equation 22 is always 1. When the secondary-side resonant elements L_{r2} and C_{r2} of the resonator are equivalent to the primary-side resonant elements L_{r1} and C_{r1} of the resonator, $h = g = 1$, the corresponding relationship between voltage gain M, quality factor Q, and normalized resonant frequency ω_n can be obtained from Equation 22, as shown in Figure 11.

According to $Q = Z_r/Z_{eq}$, when the equivalent parameter Z_r of the primary edge resonator is determined, the quality factor is inversely proportional to the equivalent load impedance. From Figure 11, the voltage gain M can be increased by appropriately reducing the converter operating frequency under a light load condition. When the load is constant, the voltage gain decreases gradually with the increase in the working frequency and finally reaches a stable value. When the converter is overloaded, the voltage gain M increases gradually with the decrease in the switching frequency. When $\omega_n < 0.5$, the voltage gain decreases rapidly and finally approaches 0. When $\omega_n = 1$, the voltage gain of the load-independent converter is always 1. When $\omega_n > 1$, the converter works under the over-resonant condition and the voltage gain value basically remains unchanged under the overload condition and gradually decreases with the decrease in load under the light load condition. The voltage gain value under the over-resonant condition is always less than 1. In the design of the resonator, considering the full load of the converter, the characteristic impedance Z_r of the original side is reduced as far as possible to obtain a smaller quality factor and a more ideal voltage gain value.

To sum up, the side resonant elements of the resonator have an impact on the voltage gain. In order to meet the voltage gain requirements when the converter runs in reverse, the resonator should be designed with a completely symmetric structure ($h = g = 1$). When the voltage gain is determined, a larger value of K and quality factor Q is selected as far as possible to ensure that the converter meets the power demand in a wider frequency range.

5 Design of the converter resonator

The above analysis shows that the voltage gain curve of the converter contains functions of ω_n, k, Q, g, and h. In the design process of the resonator, the voltage gain of the converter running in reverse is taken as $h = g = 1$, which means that the resonator is completely symmetric. In the design process, ω_n, Q, and k are the key parameters affecting the performance of the converter. ω_n is selected as the control variable, which means that the voltage gain curve remains monotonic within the operating frequency range of the demand and meets the voltage gain requirements under all load conditions in the forward and backward operation modes. In addition, the ZVS condition should be satisfied. The resonator elements are determined by optimizing the quality factor Q and the resonant inductance ratio k.

The three-port converter high-voltage side input voltage is 537 V, and the voltage fluctuation range is 525–550 V; the medium-voltage side rated output voltage is 375 V, and the voltage fluctuation range is 350–400 V; the medium-voltage side output power is 18 kW, and the working frequency is 2 kHz. After the above analysis, different values of parameters k and Q were found to affect the voltage gain of the converter. In the ideal case, the transformer ratio is determined. The DC voltage gain is set as 1; when the converter works at the quasi-resonant frequency normalized resonant frequency, $\omega_n = 1$, and the transformer theoretical ratio is determined as shown in Equation 23.

$$\boldsymbol{n} = \frac{\boldsymbol{U}_{\mathbf{in}}}{\boldsymbol{U}_{\mathbf{out1}}}. \tag{23}$$

The voltage gain values of the highest and lowest input voltages in forward operation are $M_{1\max}$ and $M_{1\min}$, respectively as shown in Equation 24.

$$\begin{cases} \boldsymbol{M}_{\mathbf{1\,max}} = \dfrac{\boldsymbol{nU}_{\mathbf{out1\_\,max}}}{\boldsymbol{U}_{\mathbf{in\_\,min}}} \\[2ex] \boldsymbol{M}_{\mathbf{1\,min}} = \dfrac{\boldsymbol{nU}_{\mathbf{out1\_\,min}}}{\boldsymbol{U}_{\mathbf{in\_\,max}}} \end{cases}. \tag{24}$$

The voltage gain values of the secondary-side highest and lowest input voltages in reverse operation are $M_{2\max}$ and $M_{2\min}$, respectively as shown in Equation 25.

$$\begin{cases} \boldsymbol{M}_{\mathbf{2\,max}} = \dfrac{\boldsymbol{U}_{\mathbf{in\_\,max}}}{\boldsymbol{nU}_{\mathbf{out1\_\,min}}} \\[2ex] \boldsymbol{M}_{\mathbf{2\,min}} = \dfrac{\boldsymbol{U}_{\mathbf{in\_\,min}}}{\boldsymbol{nU}_{\mathbf{out1\_\,max}}} \end{cases}. \tag{25}$$

The larger value of the maximum voltage gain and the smaller value of the minimum voltage gain are taken for forward and reverse operation modes. First, the impedance characteristics of the converter are analyzed. When the converter has no load, $Q = 0$, and the converter gain function taking the maximum operating frequency can be expressed as Equation 26.

$$\boldsymbol{M}(\boldsymbol{\omega}_{\mathbf{n\_\,max}}) = \frac{\mathbf{1}}{\mathbf{1} + \frac{1}{k} - \frac{1}{k\omega^2_{\mathbf{n\_\,max}}}}. \tag{26}$$

When the converter takes the minimum voltage gain $M_{\min}$, its value is greater than the no-load voltage gain $M_{\min} > M_{\text{n\_max}}$. The restriction condition of parameter k can be obtained from Equation 27.

$$\boldsymbol{k} < \frac{\boldsymbol{M}_{\mathbf{min}}}{\mathbf{1} - \boldsymbol{M}_{\mathbf{min}} \cdot \frac{\omega^2_{\mathbf{n\_\,max}}}{\omega^2_{\mathbf{n\_\,max}}}}. \tag{27}$$

Assume that the maximum operating frequency of the converter is infinite and the parameter k is the maximum value as shown in Equation 28.

$$\boldsymbol{k} < \frac{\boldsymbol{M}_{\mathbf{min}}}{\mathbf{1} - \boldsymbol{M}_{\mathbf{min}}}. \tag{28}$$

According to the parameter k limiting conditions, minimum voltage gain $M_{\min}$, $\omega_{\text{nmax}} = 2\pi f_{\max}/2\pi f_r = f_{\text{nmax}}$, and normalized quasi-resonant frequency $f_{\text{nmax}} = f_{\max}/f_r$, the maximum operating frequency of the converter can be determined as shown in Equation 29.

$$\boldsymbol{f}_{\mathbf{nmax}} = \frac{\mathbf{1}}{\sqrt{\mathbf{1} + \boldsymbol{k}\left(\mathbf{1} - \frac{1}{M_{\mathbf{min}}}\right)}}. \tag{29}$$

According to Equation 28, the maximum k value is 10 when the converter has no load. When $k = 10$, the frequency range of the converter is too wide, which is inconsistent with the actual operation of the converter. Considering the forward and backward operation modes of the converter, the maximum normalized resonant frequency $f_{\text{nmax}} = 1.25$ is taken from Equation 29, and the k value is 3.68.

The condition of the converter to realize ZVS is the switching tube current hysteresis voltage, which is the equivalent input impedance of the inductive resonator. According to Figure 9, the input impedance of the simplified model of the converter fundamental wave can be expressed as Equation 30.

$$\boldsymbol{Z}_{\text{in}}(\boldsymbol{\omega}_{\mathbf{n}}) = \boldsymbol{Z}_{\mathbf{1}} + \boldsymbol{Z}_{\mathbf{m}} // \left(\boldsymbol{Z}_{\mathbf{2}} + \boldsymbol{R}_{\text{eq}}\right). \tag{30}$$

According to the characteristic impedance Z_r and inductance coefficient k, the normalized parameter is $g = h = 1$; the normalized input impedance $Z_n = Z_{in}/Z_r$ can be expressed as

$$\begin{aligned} \boldsymbol{Z}_{\mathbf{n}}(\boldsymbol{\omega}_{\mathbf{n}}) = {} & \frac{\boldsymbol{Qk\omega}^6_{\mathbf{n}} - \boldsymbol{j}\left(\boldsymbol{\omega}_{\mathbf{n}} - (\boldsymbol{k}+\mathbf{1})\boldsymbol{\omega}^3_{\mathbf{n}}\right)}{\boldsymbol{\omega}^4_{\mathbf{n}} + \boldsymbol{Q}^2\left(\boldsymbol{\omega}_{\mathbf{n}} - (\boldsymbol{k}+\mathbf{1})\boldsymbol{\omega}^3_{\mathbf{n}}\right)^2} \\ & + \frac{\boldsymbol{Q}^2\left(\left((\mathbf{2}\boldsymbol{k}+\mathbf{1})\boldsymbol{\omega}^2_{\mathbf{n}} - \mathbf{1}\right)\left(\boldsymbol{\omega}^2_{\mathbf{n}} - \mathbf{1}\right) + \boldsymbol{\omega}^2_{\mathbf{n}}\right.}{\boldsymbol{\omega}^4_{\mathbf{n}} + \boldsymbol{Q}^2\left(\boldsymbol{\omega}_{\mathbf{n}} - (\boldsymbol{k}+\mathbf{1})\boldsymbol{\omega}^3_{\mathbf{n}}\right)^2}. \end{aligned} \tag{31}$$

The condition for the converter to realize ZVS is the switching tube current hysteresis voltage, and the equivalent input impedance is the sensitivity. When the converter is just in the ZVS region, it means that the equivalent input impedance is purely resistive, the phase of the current and voltage is equal, and the imaginary part of Equation 31 is 0, which means that the equivalent input impedance is the dividing line of the inductive capacitance.

$$\begin{aligned} \text{Im}\left[\boldsymbol{Z}_{\mathbf{n}}(\boldsymbol{\omega}_{\mathbf{n}})\right] = {} & \frac{\left((\boldsymbol{k}+\mathbf{1})\boldsymbol{\omega}^2_{\mathbf{n}} - \mathbf{1}\right)}{\boldsymbol{\omega}^3_{\mathbf{n}} + \boldsymbol{Q}^2\left(\mathbf{1} - (\boldsymbol{k}+\mathbf{1})\boldsymbol{\omega}^2_{\mathbf{n}}\right)^2} \\ & + \frac{\boldsymbol{Q}^2\left(\left((\mathbf{2}\boldsymbol{k}+\mathbf{1})\boldsymbol{\omega}^2_{\mathbf{n}} - \mathbf{1}\right)\left(\boldsymbol{\omega}^2_{\mathbf{n}} - \mathbf{1}\right) + \boldsymbol{\omega}^2_{\mathbf{n}}\right.}{\boldsymbol{\omega}^3_{\mathbf{n}} + \boldsymbol{Q}^2\left(\mathbf{1} - (\boldsymbol{k}+\mathbf{1})\boldsymbol{\omega}^2_{\mathbf{n}}\right)^2}. \end{aligned} \tag{32}$$

According to Equation 32, when the imaginary part of the normalized impedance is 0, two constraints Equations 33, 34 are obtained. In order to realize the converter ZVS and the maximum gain $M_{\max}$, the Q-value selection and the minimum operating frequency $f_{\min}$ are discussed.

$$(\boldsymbol{k}+\mathbf{1})\boldsymbol{\omega}^2_{\mathbf{n}} = \mathbf{1}, \tag{33}$$

$$\boldsymbol{Q}^2\left(\left((\mathbf{2}\boldsymbol{k}+\mathbf{1})\boldsymbol{\omega}^2_{\mathbf{n}} - \mathbf{1}\right)\left(\boldsymbol{\omega}^2_{\mathbf{n}} - \mathbf{1}\right) + \boldsymbol{\omega}^2_{\mathbf{n}} = \mathbf{0}. \tag{34}$$

If Equation 33 is established, it can be concluded that when the equivalent impedance is purely resistive, $\omega_n = 1/\sqrt{k+1}$, the equivalent input impedance of the converter is purely resistive so the operating frequency range of the converter is limited to $1/\sqrt{k+1} < \omega_n < 1$.

If Equation 34 is established, the expression of quality factor $Q_{\max}$ can be obtained:

$$\boldsymbol{Q}(\boldsymbol{\omega}_{\mathbf{n}})_{\mathbf{max}} = \sqrt{\frac{\boldsymbol{\omega}^2_{\mathbf{n}}}{\left(\mathbf{1} - \boldsymbol{\omega}^2_{\mathbf{n}}\right)\left((\mathbf{2}\boldsymbol{k}+\mathbf{1})\boldsymbol{\omega}^2_{\mathbf{n}} - \mathbf{1}\right)}}. \tag{35}$$

Substituting Equation 35 into the voltage gain expression Equation 21 yields the minimum normalized frequency at the maximum voltage gain as shown in Equation 36:

$$\boldsymbol{f}_{\mathbf{nmin}} = \frac{\mathbf{1}}{\sqrt{\mathbf{1} + \boldsymbol{k}\left(\mathbf{1} - \frac{1}{M^2_{\mathbf{max}}}\right)}}, \tag{36}$$

For $k = 3.5$, the relationship between the maximum and minimum gain of voltage gain and the converter is shown in Figure 12.

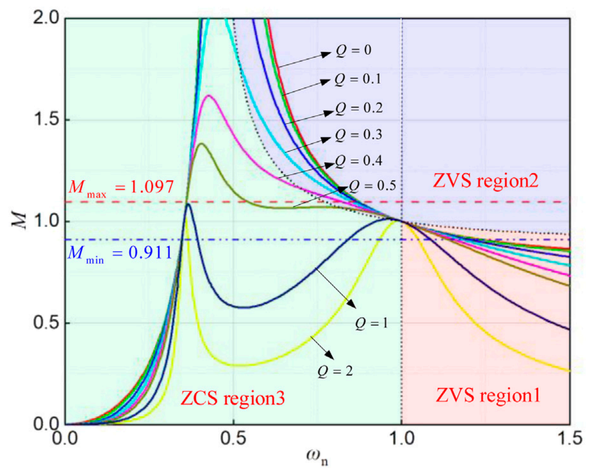

FIGURE 12
Voltage gain curves at different Q-values.

As the normalized equivalent impedance is inductive in region 1, the AC square wave voltage across the converter resonator leads a resonant current so that power switches reach ZVS. In region 2, where the normalized equivalent impedance is inductive as well, the switch tube reaches ZVS, and rectifier diodes on the rectifier side reach ZCS. Contrastingly, in region 3, characterized by capacitive normalized equivalent impedance, the switch tube fails to achieve ZVS, and it can be observed that the voltage gain has a large variation within this region. Therefore, different Q-values should be avoided in region 3 when designing the converter resonator.

According to Equation 33, the normalized frequency of the converter is limited to the range $1/\sqrt{k+1} < \omega_n < 1$. According to the ZVS realization of the converter, the normalized characteristic impedance is inductive. In this case, the quality factor Q is limited to

$$Q^2(\omega_n) < \frac{\omega_n^2}{(1-\omega_n^2)\left((2k+1)\omega_n^2 - 1\right)}. \tag{37}$$

Let $F(\omega_n) = Q^2(\omega_n)$ and find the derivative. The derivative function is equal to 0. The operating frequency ω_0 is found within the operating frequency range $1/\sqrt{k+1} < \omega_n < 1$, and quality factor Q takes the extreme value.

$$\begin{cases} F(\omega_n) = \dfrac{\omega_n^2}{(1-\omega_n^2)\left((2k+1)\omega_n^2 - 1\right)} \\ F'(\omega_n) = \dfrac{2\omega_n\left((2k+1)\omega_n^4 - 1\right)}{(1-\omega_n^2)^2\left((2k+1)\omega_n^2 - 1\right)^2} \end{cases}. \tag{38}$$

According to Equation 38, when $\omega_0 = 1/\sqrt[4]{2k+1}$, Q_{max} takes the extreme value, and the restriction condition of quality factor Q_{max} can be obtained by substituting it into Equation 37 as shown in Equation 39.

$$Q_{max} < \frac{1}{\sqrt{2k+1} - 1}. \tag{39}$$

The converter operating frequency range is $1/\sqrt[4]{2k+1} < \omega_n < 1$. A reasonable Q-value is selected, and it is verified that when $\omega_0 = 1/\sqrt[4]{2k+1}$, the voltage gain is greater than M_{max}; if not, the conditions are met and the Q-value is reduced.

According to Equation 23, the transformer ratio is 1.432. The forward and reverse operation voltage gains are $M_{1max} = 1.091$, $M_{1min} = 0.0911$, $M_{2max} = 1.097$, and $M_{2min} = 0.0917$.

After comprehensive consideration, the parameter is $k = 3.5$, and the maximum quality factor Q is calculated as 0.546. When $Q = 0.4$, the voltage gain is 1.249, which meets the demand.

Load resistance R_0 and equivalent resistance R_{eq} are calculated as follows:

$$\begin{cases} R_0 = \dfrac{{U_{out1}}^2}{P_{out1}} \\ R_{eq} = n^2 \dfrac{8}{\pi^2} R_0 \end{cases}. \tag{40}$$

According to Equation 40, the load resistance and equivalent resistance are 7.812 Ω and 12.99 Ω, respectively. The maximum and minimum resonant frequencies of the converter during rated operation are determined as follows:

$$\begin{cases} f_{min} = \dfrac{f_r}{\sqrt{1 + k\left(1 - \dfrac{1}{{M_{max}}^2}\right)}} \\ f_{max} = \dfrac{f_r}{\sqrt{1 + k\left(1 - \dfrac{1}{M_{min}}\right)}} \end{cases}. \tag{41}$$

Equation 41 shows that the maximum resonant frequency of the converter is 1.585 kHz and the minimum resonant frequency is 2.465 kHz. Based on the quality factor, the resonant inductance and the resonant capacitance of the primary side of the resonator can be calculated as shown in Equations 42, 43.

$$Q = \frac{Z_r}{Z_{eq}} = \frac{\sqrt{\frac{L_{r1}}{C_{r1}}}}{R_{eq}} = \frac{2\pi f_{r1} L_{r1}}{R_{eq}}, \tag{42}$$

$$\begin{cases} L_{r1} = \dfrac{QR_{eq}}{2\pi f_{r1}} \\ C_{r1} = \dfrac{1}{2\pi f_{r1} R_{eq} Q} \end{cases}. \tag{43}$$

The resonant inductance and capacitance of the resonator's secondary side are calculated as Equation 44.

$$\begin{cases} L_{r2} = L_{r1}/n^2 \\ C_{r2} = n^2 C_{r1} \end{cases}. \tag{44}$$

The resonator element is calculated as $L_{r1} = 0.6$ mH, $C_{r1} = 11$ μF, $L_{r2} = 0.29$ mH, and $C_{r2} = 22$ μF.

Figure 13 shows the corresponding relationship between the voltage gain curve and normalized resonant frequency during forward and reverse operation modes. From Figure 13, the working frequencies of the forward and reverse running processes can be determined.

After discussing the value of parameters k and Q, from Figure 13, when the converter runs in the positive and negative directions, the voltage gain in the range of the under-resonant operating frequency meets the requirements.

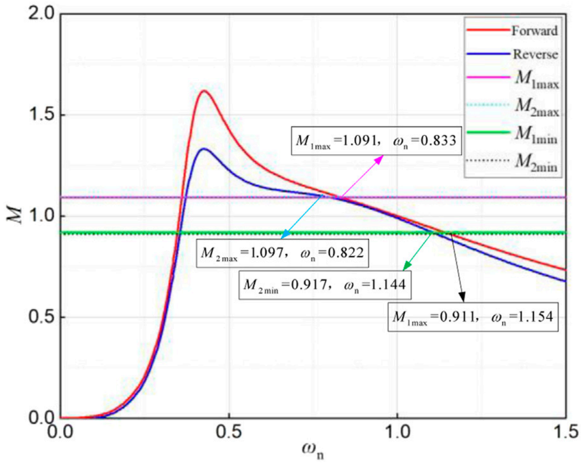

FIGURE 13
Voltage gain curve at the converter positive and negative operation modes.

6 The simulation verification

In order to verify the rationality of theoretical analysis and parameter design, PSIM simulation software is used to simulate the forward operation of the three-port DC–DC converter under ω_n = 0.9 and different load conditions. Figure 14A shows the driving waveforms of the converter switch S_1 and S_3, and Figure 14B shows the waveforms of the input voltage U_{in} of the resonator and the voltage U_{Lm} of the excitation inductor.

Figure 15 shows the current waveforms of excitation inductors L_m and the original and secondary-side resonant inductors L_{r1} and L_{r2} under different load conditions when ω_n = 0.9. Figure 15 shows that the resonant currents i_{Lr1} and i_{Lr2} lag behind the excitation current i_{Lm}, and the switch tube realizes ZVS.

Figure 16 shows the waveforms of the input current i_{pri} and output current i_{sec} of the resonator under light-load and full-load conditions. When the load increases, the original and secondary side currents meet the power transmission requirements.

Figure 17 illustrates the output current waveform of port 2 in the three-port converter under both light-load and full-load conditions in a steady state. Figure 18 shows the resonant capacitor current waveforms on the input side and output side of the resonator under light-load and full-load conditions. The figure shows that the voltage and current of the three-port DC/DC converter can meet the power transmission requirements under both light-load and full-load conditions.

Figure 19 shows that the fixed port 1 input voltage is 537 V, and the output voltage of port 2 and port 3 is stable. U_{out1} and U_{out2} are stable at 375 and 48 V, respectively, when the converter runs forward.

The simulation study of the forward operation of the converter under different loads shows that the voltage and current waveforms of the resonator components meet the power output requirements, and the parameters of the resonator components are reasonable. In order to further verify the rationality of the resonator design, simulation research was conducted on the reverse operation of the converter. The fixed reverse input voltage was 375 V, and the resonator current and voltage waves during the reverse operation of the converter are shown in Figure 20.

The voltage and the current values of the resonator elements are stable in the forward and reverse operation modes, and the converter can meet the power output requirements under different loads.

Figure 21 shows the curve of DC voltage gain G_{dc} with normalized frequency during the forward and reverse operation modes of the converter.

The simulation results given in Figure 21 show that the forward and reverse operation modes of the converter reach the calculated value of voltage gain. The simulation of the forward and reverse operation modes of the converter verified that the resonant cavity parameters of the converter meet the design requirements under the premise of voltage gain and power transmission and realize ZVS in the under resonant range. ZVS implementation is shown in Figure 22.

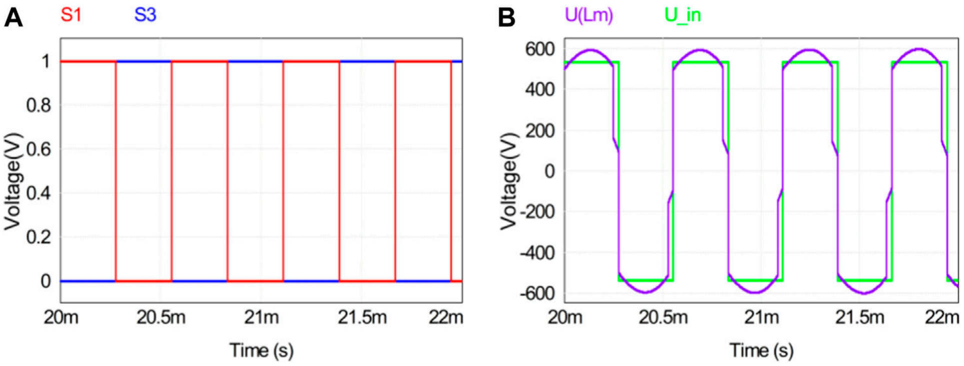

FIGURE 14
Switching drive and input voltage waveforms. **(A)** Switch tube drive waveform. **(B)** Input voltage of the resonator.

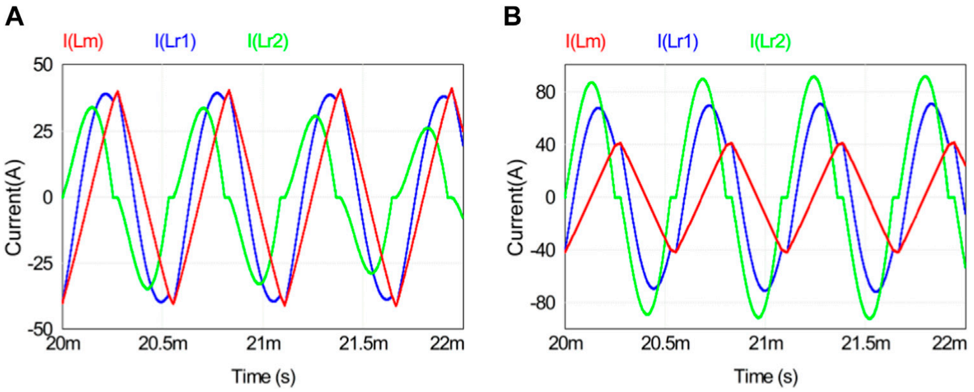

FIGURE 15
Current waveforms under different loads: **(A)** light load and **(B)** heavy load.

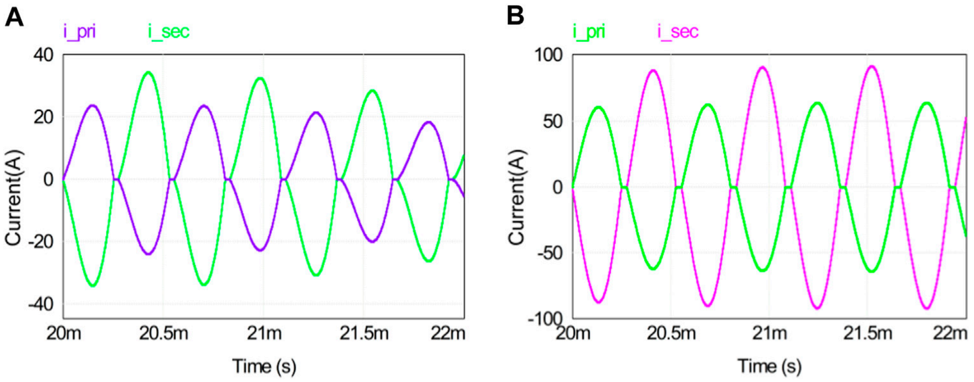

FIGURE 16
Resonant current waveforms of the converter at different loads: **(A)** light load and **(B)** heavy load.

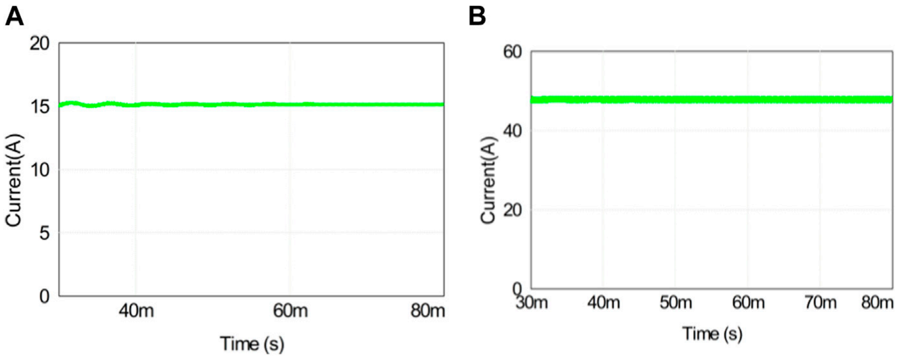

FIGURE 17
Port 2 output current waveforms at different loads: **(A)** light load and **(B)** heavy load.

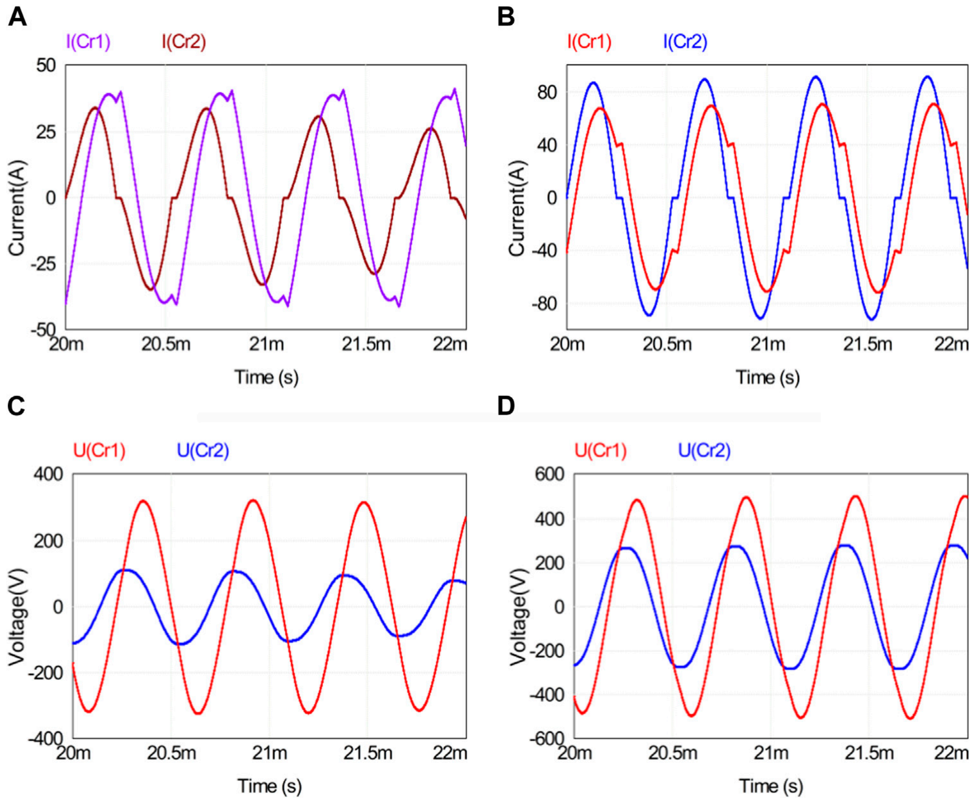

FIGURE 18
Resonant capacitor current and voltage waveforms at different loads: **(A)** light-load current waveform; **(B)** full-load current waveform; **(C)** light-load voltage waveform; **(D)** full-load voltage waveform.

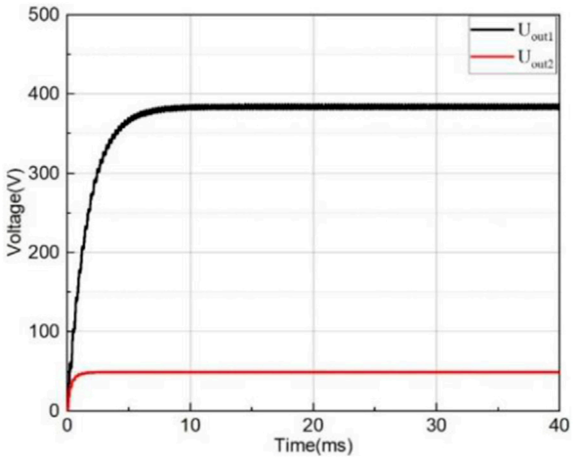

FIGURE 19
Output voltage waveforms of the converter.

7 Experiment research

On account of the above theoretical analysis and simulation investigation, a 20-kW three-port DC–DC converter experimental platform is established, as shown in Figure 23. TMS320F28335 is selected as the main control chip to validate the rationality of this design scheme.

Figure 24 shows the driving output waveform of the converter switch S_1, where V_{gs_S1} and V_{ds_S1} are the gate voltage and drain voltage of the switch S_1, respectively. The figure shows that the switch tube implements ZVS.

The output voltage waveforms of the medium- and low-voltage sides of the three-port DC–DC converter are shown in Supplementary Figure S1. The figure shows the stability of the output voltages at 375 and 48 V, affirming the validity of the proposed scheme.

8 Conclusion

Addressing the shortage of distributed power supply and the DC distribution network in domestic and abroad situations, this paper proposes a three-port DC-DC converter topology based on a low-voltage DC distribution network, which can effectively combine distributed energy, low-voltage load, and the DC bus. This research analyzes different energy transfer modes of the three-port DC–DC converter, and decoupling analysis is carried out on the main circuit topology structure. The working process of the equivalent model of the three-port DC–DC converter in the first half cycle of four time stages is analyzed in detail when the energy flow is forward. Then, the characteristics of the converter are studied. Based on the fundamental equivalent analysis method, the simplified equivalent model of the converter is established and the resonant frequency characteristics and voltage gain characteristics of the converter are analyzed. According to the different voltage gains,

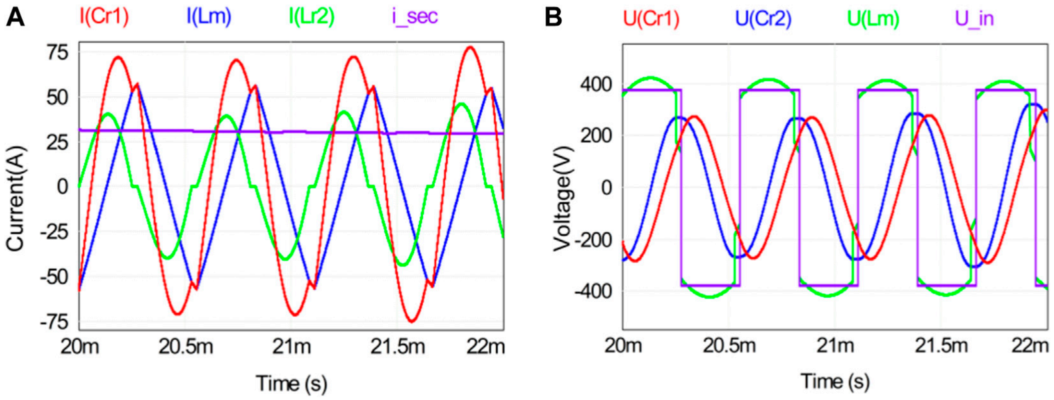

FIGURE 20
Reverse operation voltage and current waveforms: **(A)** current waveform and **(B)** voltage waveform.

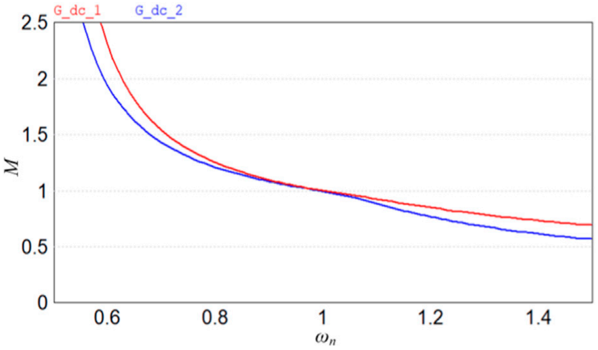

FIGURE 21
Voltage gain curves of forward and reverse operation.

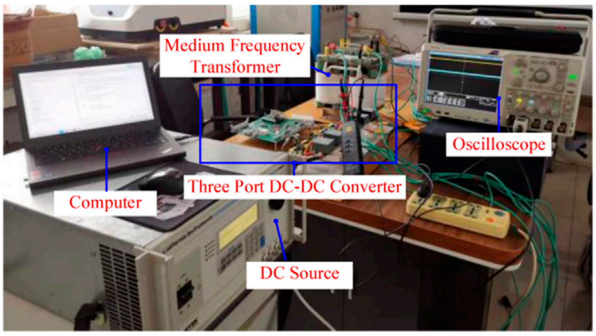

FIGURE 23
Experimental system of the three-port DC–DC converter.

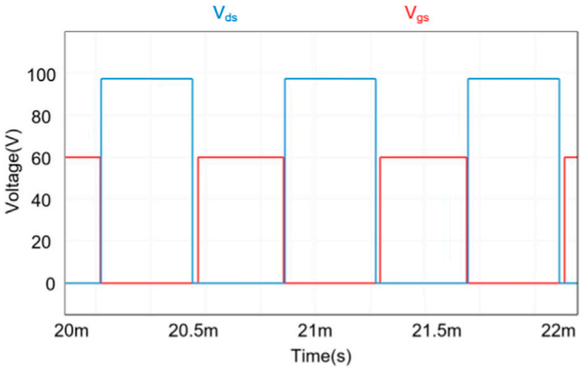

FIGURE 22
Implementation of ZVS

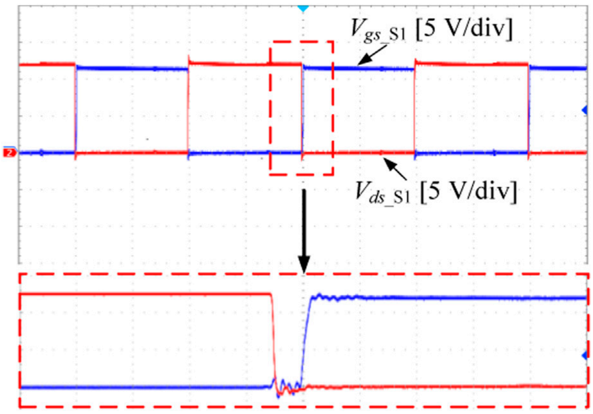

FIGURE 24
Waveform of the switch S_1 driver.

the influence of different values of the converter parameters k and Q on the gain characteristics of the converter is analyzed, and the design of the resonator is completed by choosing the parameters k and Q reasonably. Based on the theoretical derivation and using PSIM simulation software, the forward and reverse operation modes of the converter under different load conditions are simulated and analyzed. The experimental platform of a 20-kW three-port DC–DC converter is built, and experimental investigations are conducted under varied load conditions. The experimental results show that the converter can achieve stable power output under different working conditions. The use of ultra-thin silicon steel sheets in high-power intermediate-frequency applications can effectively reduce the total loss of intermediate-frequency transformers, thereby providing additional confirmation regarding the correctness and feasibility of the proposed scheme for a high-power medium-frequency converter with ultra-thin silicon steel sheets.

Data availability statement

The original contributions presented in the study are included in the article/Supplementary Material; further inquiries can be directed to the corresponding authors.

Author contributions

LH: conceptualization, project administration, resources, and writing–original draft. MZ: conceptualization, investigation, software, visualization, and writing–review and editing. YW: data curation, methodology, resources, visualization, and writing–review and editing. FQ: supervision, validation, and writing–review and editing. DS: formal analysis, investigation, writing–review and editing. XY: formal analysis, methodology, and writing–review and editing. YL: data curation and writing–original draft. ZY: project administration, validation, and writing–review and editing.

Funding

The author(s) declare that financial support was received for the research, authorship, and/or publication of this article. This research was funded by the State Grid Corporation of China (No. kj2021-040), "Development of Intelligent Control Technology and Platform for City Integral Energy System in Xiong'an New Area."

Conflict of interest

Authors LH, FQ, DS, and XY were employed by State Grid Hebei Electric Power Co., Ltd. Author MZ was employed by State Grid Hebei Service Center Co., Ltd. Author YW was employed by Shanghai Electric Power Design Institute Co., Ltd. Author YL was employed by XJ Group Corporation.

The remaining author declares that the research was conducted in the absence of any commercial or financial relationships that could be construed as a potential conflict of interest.

The authors declare that this study received funding from State Grid Corporation of China. The funder had the following involvement in the study: design, collection, analysis, interpretation of data, the writing of this article, and the decision to submit it for publication.

Publisher's note

Supplementary material

The Supplementary Material for this article can be found online at: https://www.frontiersin.org/articles/10.3389/felec.2024.1369905/full#supplementary-material

References

Bahmani, A. M., Thiringer, T., and Kharezy, M. (2016). "Optimization and experimental validation of medium-frequency high power transformers in solid-state transformer applications," in 2016 IEEE applied power electronics conference and exposition (APEC), Long Beach, CA, USA, March 20–24, 2016 (IEEE), 3043–3050.

Boroyevich, D., Cvetkovic, I., Dong, D., Burgos, R., Wang, F., and Lee, F. (2010). "Future electronic power distribution systems a contemplative view," in 12th international conference on optimization of electrical and electronic equipment (OPTIM), Brasov, Romania, May 20–22, 2010 (IEEE), 1369–1380.

Chen, Y. (2017). *Design of DC/DC converter and research on stable operation technology of DC distribution network. Master's degree*. Beijing China: North China Electric Power University.

Heinemann, L. (2002). "An actively cooled high power, high frequency transformer with high insulation capability," in 17th annual IEEE applied power electronics conference and exposition (APEC), Dallas, USA, March 10–14, 2002 (IEEE), 352–357.

Ortiz, G., Biela, J., and Kolar, J. W. (2010). "Optimized design of medium frequency transformers with high isolation requirements," in IECON 2010-36th annual conference of the IEEE industrial electronics society, Glendale, USA, November 7–10, 2010 (IEEE), 631–638.

She, X., Huang, A. Q., and Burgos, R. (2013). Review of solid-state transformer technologies and their application in power distribution systems. *IEEE J. Emerg. Sel. Top. Power Electron.* 1 (3), 186–198. doi:10.1109/JESTPE.2013.2277917

Soltau, N., Eggers, D., Hameyer, K., and Doncker, R. (2014). Iron losses in a medium-frequency transformer operated in a high-power DC–DC converter. *IEEE Trans. Magn.* 50 (2), 953–956. doi:10.1109/TMAG.2013.2283733

Song, Q., Liu, W., Li, X., Rao, H., Xu, S., and Li, L. (2013). A steady-state analysis method for a modular multilevel converter. *IEEE Trans. Power Electron.* 28 (8), 3702–3713. doi:10.1109/tpel.2012.2227818

Tong, Y. B., Tong, W. U., Jin, X. M., and Chen, Y. (2007). Study of bi-directional dc/dc converter. *Proc. CSEE* 27 (13), 81–86. doi:10.3321/j.issn:0258-8013.2007.13.015

Villar, I., Rufer, A., Viscarret, U., Zurkinden, F., and Etxeberria-Otadui, I. (2008). "Analysis of empirical core loss evaluation methods for non-sinusoidally fed medium frequency power transformers," in 2008 IEEE international symposium on industrial electronics (ISIE), Cambridge, United Kingdom, June 30–July 2, 2008 (IEEE), 208–213.

Villar, I., Viscarret, U., Etxeberria-Otadui, I., and Rufer, A. (2009). Global loss evaluation methods for nonsinusoidally fed medium-frequency power transformers. *IEEE Trans. Ind. Electron.* 56 (10), 4132–4140. doi:10.1109/TIE.2009.2021174

Wu, T. F., Chang, C. H., Lin, L. C., Yu, G. R., and Chang, Y. R. (2013). DC-bus voltage control with a three-phase bidirectional inverter for DC distribution systems. *IEEE Trans. Power Electron.* 28 (4), 1890–1899. doi:10.1109/TPEL.2012.2206057

Zhao, Y., Zheng, J., Zhang, Z., Shi, D., Qin, X., Shao, J., et al. (2021). "Influence of amorphous fragment on eddy current field of amorphous alloy transformer," in 2021 IEEE international conference on power electronics computer applications (ICPECA), Shenyang, China, January 22–24, 2021 (IEEE), 497–501.

Zheng, H. (2014). *Research on some Problems of flexible DC distribution network. Master's Degree*. Zhejiang China: Zhejiang University.